FULL PAPER

Molecular Junctions Composed of Oligothiophene Dithiol-Bridged Gold Nanoparticles Exhibiting Photoresponsive Properties

Wei Huang,*[a, b] Gou Masuda,[c] Seisuke Maeda,[c] Hirofumi Tanaka,[a, d] and Takuji Ogawa*[a, d]

Abstract: Three oligothiophene dithiols with different numbers of thiophene rings (3, 6 or 9) have been synthesized and characterized. The X-ray single crystal structures of terthiophene **2** and sexithiophene **5** are reported herein to show the exact molecular lengths, and to explain the difference between their UV-visible spectra arising from the different packing modes. These dithiols with different chain lengths were then treated with 2-dodecanethiol-protected active gold nanoparticles (Au-NPs) by means of in situ thiol-to-thiol ligand exchange in the presence of 1 μm gap Au electrodes. Thus the molecular junctions composed of self-assembled films were prepared, in which oligothio-phene dithiol-bridged Au-NPs were attached to two electrodes by means of Au−S bonded contacts. The morphologies and current–voltage (*I–V*) characteristics of these films were studied by SEM and AFM approaches, which suggested that the thickness of the films (3–4 layers) varied within the size of one isolated Au-NP and typical distance-dependent semiconductor properties could be observed. Temperature dependent *I–V* measurements for these molecular junctions were performed in which the films served as active elements in the temperature range 6–300 K; classical Arrhenius plots and subsequent linear fits were carried out to give the activation energies (ΔE) of devices. Furthermore, preliminary studies on the photoresponsive properties of these devices were explored at 80, 160, and 300 K, respectively. Physical and photochemical mechanisms were used to explain the possible photocurrent generation processes. To the best of our knowledge, this is the first report in which oligothiophene dithiols act as bridging units to link Au-NPs, and also the first report about functionalized Au-NPs exhibiting photoresponse properties in the solid state.

Keywords: gold · nanostructures · oligothiophenes · photoresponse · semiconductors · thin films

Introduction

Molecular electronics is a fairly new and fascinating area of research that is firing the imagination of scientists as few research topics have in the past, and significant advances have been made during the last a few years in various applications of nanotechnology.[1–3] In general, it involves the search for single molecules or small groups of molecules that can be used as the fundamental units or self-contained electronic devices, that is, wires, switches, and memory and gain elements. The goal is to use these molecules, designed from the bottom-up to have specific properties and behaviors, instead of present solid-state electronic devices that are constructed by lithographic technologies from the top-down.[4] In recent

[a] Dr. W. Huang, Dr. H. Tanaka, Prof. Dr. T. Ogawa
Research Center for Molecular Nanoscience
Institute for Molecular Science
National Institutes of Natural Sciences
5-1 Higashiyama, Myodaiji-cho, Okazaki
Aichi, 444-8787 (Japan)
Fax: (+81) 564-59-5635
E-mail: whuang@nju.edu.cn
ogawat@ims.ac.jp

[b] Dr. W. Huang
State Key Laboratory of Coordination Chemistry
Coordination Chemistry Institute
Nanjing University, Nanjing 210093 (China)

[c] G. Masuda, S. Maeda
Department of Chemistry, Faculty of Science
Ehime University, Bunkyo-cho 2-5, Matsuyama
Ehime, 790-8577 (Japan)

[d] Dr. H. Tanaka, Prof. Dr. T. Ogawa
Core Research for Evolutional Science and Technology (CREST)
Japan Science and Technology Agency (JST)
Hon-machi 4-1-8, Kawaguchi, Saitama, 332-0012 (Japan)

years, several research groups have reported the measurements of the current–voltage (*I–V*) characteristics of self-assembled monolayers (SAMs) of conjugated polymers,[5–7] as they have potential applications in semiconductor nanotechnology. In view of the intrinsic difficulties and fragility demonstrated by single-molecular or SAM junctions, well-defined self-assembled thin films formed between micro-gap Au electrodes, in the presence of Au-NPs, are reported herein. The resultant films exhibit good and reproducible *I–V* curves; hence, it is possible for us to discuss the possible conduction mechanism on the nanometer scale, which is still a poorly understood field.[8]

It is known that thiol groups can be chemisorbed onto gold surfaces strongly and that they can be used as a protected species to synthesize functionalized, ligand-stabilized Au-NPs. Brust et al[9] developed a general approach for the preparation of thiol-protected Au-NPs with a narrow size distribution; this method is based on the reduction of $AuCl_4^-$ in toluene with an aqueous $NaBH_4$ solution in the presence of certain phase-transfer catalysts. More importantly, it is also possible for terminal dithiols to replace the protecting thiol groups through thiol-to-thiol ligand-exchange reactions. If gold electrodes are used, thiol groups can be further absorbed chemically to form molecular junctions. As a result, a variety of electro-optical devices can be fabricated successfully in this way. In previous work, we showed that stable arrays of 1,10-decanedithiol-bridged Au-NPs could be easily obtained between a pair of Au-electrodes.[10] This material demonstrated semiconductor-like properties with characteristic sigmoidal-shaped *I–V* curves and a linear $\log(I)$ versus $1/T$ relationship when attached to gold microelectrodes, in contrast with the bulk material which showed ohmic behavior.

For a given metal/dielectric-film/metal system, certain conduction mechanisms may dominate in certain voltage and temperature regimes. So it is interesting to study their electronic correlation of voltage and temperature. We have recently reported the *I–V* characteristics of molecular nanodevices in which a polymer of an Ru[II] complex bearing the 3,8-bis[terthiophenyl-(1,10-phenanthroline)] ligand was electrodeposited as functionalized molecular wires between nanogap (~15 nm) electrodes.[11] Our strategy here is first to prepare monothiol-potected active Au-NPs, in which the monothiol (2-dodecanethiol) serves as a surfactant capping molecule (the average size of them in our case is 3.3 ± 1.0 nm), and then use a thiol-to-thiol exchange reaction to replace the monothiol with different dithiols, and finally bridge a micro-gap source and drain electrodes by means of a self-assembly method. Accordingly, metal–film–metal junctions can be produced on the molecular level composed of dithiol-bridged Au-NPs. Polythiophenes and oligothiophenes have been widely studied as conducting polymers when doped, because they contain extensive conjugated π-electron systems and they are much more stable than polyacetylene films toward oxidative degradation.[12] However, they have not been involved in the research of self-assembly with Au-NPs to fabricate nanodevices. In this paper, we

report the syntheses and characterization of three thiocyano-terminated oligothiophene precursors and their respective dithiols; the subsequent self-assembly with Au-NPs for fabricating molecular junctions (Figure 1), with characterization of the formed films by SEM and AFM methods; and the *I–V* characteristics and photoresponse properties of the fillms.
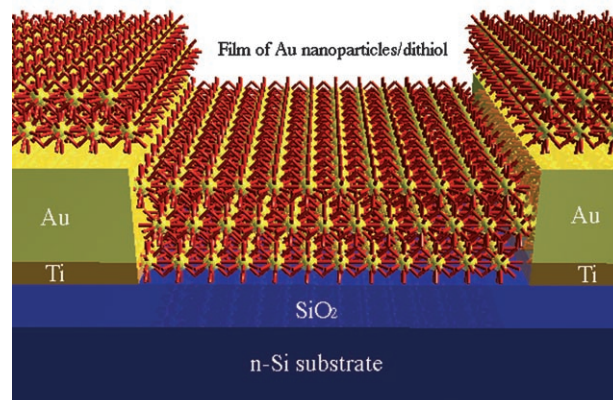

Figure 1. Schematic diagram of a self-assembled film consisting of dithiol-bridged active Au-NPs between 1 μm gap Au electrodes with photoresponse properties.

Results and Discussion

Synthesis: Oligothiophenes with different lengths capped by thiocyano groups were obtained after a multistep synthesis (Scheme 1). Different molar ratios of *N*-bromosuccinimide (NBS) and 3′,4′-dibutyl-2,2′:5′,2″-terthiophene were used to synthesize the mono- and dibromination products **3** and **6**, respectively. Compound **2** was obtained by a Ni-catalyzed cross-coupling to 2,5-dibromo-3,4-dibutylthiophene and subsequent reaction with Br_2 and KSCN to give the thiocyano derivative, while compound **5** was yielded by the similar way except that terthiophene **3** was used in the coupling reaction. Compound **8** was prepared by Ni-catalyzed cross-coupling of terthiophene **6** with the appropriate Grignard reagent and subsequent thiocyanation. Three oligothiophenes end-capped by thiocyanate (**9**, **10**, and **11**) were used to fabricate devices immediately after they were reduced by $LiAlH_4$ in dry THF from their respective thiocyano precursors (**2**, **5**, and **8**), because they were readily oxidized when exposed to air. All steps gave moderate to high yields making the strategy convenient for the preparation of these functionalized oligothiophene derivatives. Except for the elemental analyses of unstable dithiols, NMR spectroscopy, mass spectrometry, and elemental analyses of the compounds were performed and are consistent with the structures shown in Scheme 1. In addition, **2** and **5** were further characterized by X-ray single-crystal diffraction.

To obtain good films, all the dithiols, the Au-NPs with narrow size distribution, and the gold electrodes were freshly prepared before use. Successful preparation of black self-assembled films (which were insoluble in chloroform and
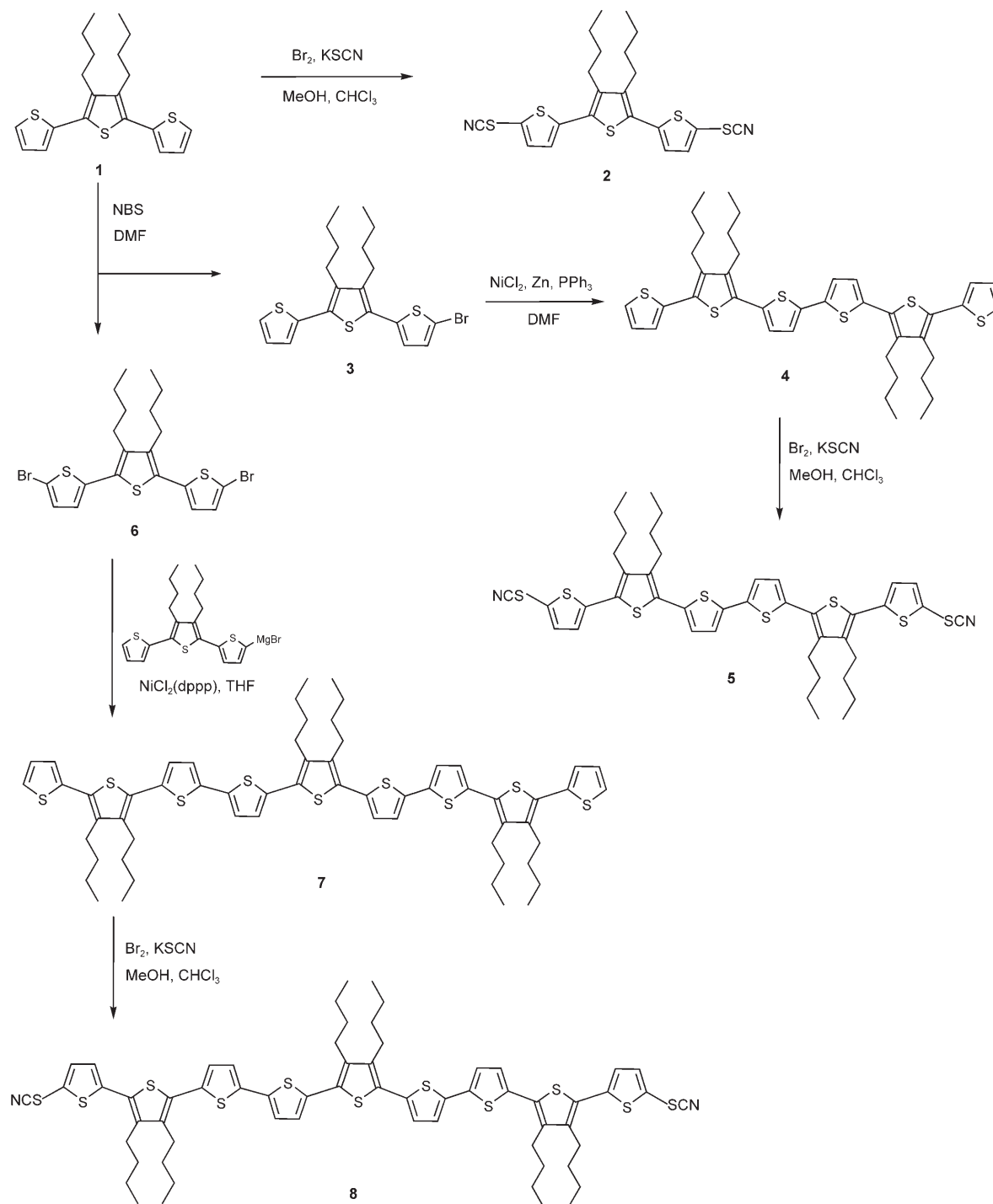
Scheme 1. Synthetic route for compounds **2**, **5** and **8**.

could be easily checked by the optical microscope and SEM) by means of thiol-to-thiol exchange reactions was verified according to the conductance between the Au-electrodes, since the contrast experiments showed that neither 2-dodecanethiol-protected Au-NPs nor dithiols only can generate current between the micro-gap electrodes. Furthermore, the presence, thickness, and I–V characteristics of the films were also characterized by AFM topographs.

Structural description of terthiophene 2 and sexithiophene 5: Drawings of the molecular structures with the atom-numbering schemes for **2** and **5** are illustrated in Figure 2. From X-ray single-crystal diffraction study, compound **2** crystallizes in the monoclinic chiral space group *Cc* and has two crystallographically unique molecules in each unit cell. Three thiophene rings adopt a *trans* conformation, but they are not coplanar. The bite angles between the side rings and
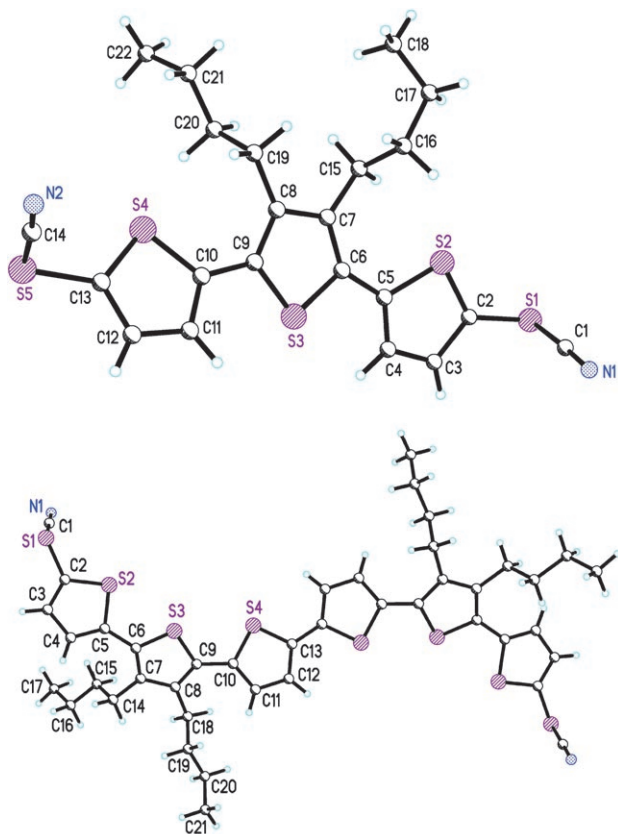
Figure 2. Ball-and-stick views of the molecular structures of **2** (top) and **5** (bottom) with the atom-numbering scheme.

the middle ring for each molecule are 14.7 and 21.9° and 16.0 and 20.1°, respectively. *n* Butyl aliphatic chains bonded to the middle thiophene rings are fully extended, also adopting the *trans* conformation to minimize the steric crowding. However, two terminal linear thiocyanate groups are found to be in a *cis* conformation with respect to the molecular plane. The crystal packing of compound **2** is shown in Figure 3.

Analysis of the single-crystal structure of **5** indicates that it crystallizes in a monoclinic system of centrosymmetric
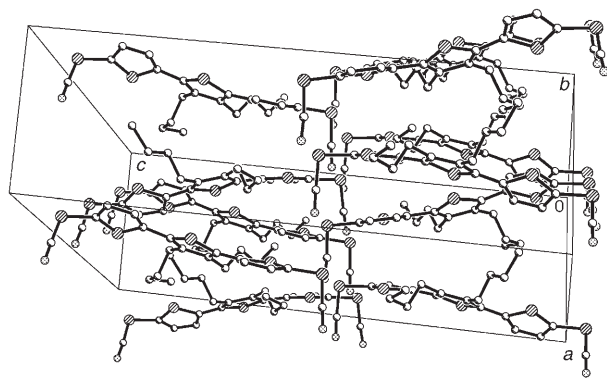
space group $P2_1/c$ and each asymmetric unit contains half of the crystallographically unique molecule. Six thiophene rings adopt a zigzag chain so that two groups of *n*-butyl side chains bound to their respective thiophene rings can be fully extended, adopting a *trans* conformation to minimize the spatial repulsion. In contrast to compound **2**, two essentially linear thiocyanate radicals (S1-C1-N1 = 177.9(7)°) adopt a *tran* conformation with respect to the molecular plane. The middle two thiophene rings are parallel with each other, but the other thiophene rings are a little twisted because of the presence of alkyl groups. The dihedral angles between the *n*-butyl-substituted thiophene rings and the adjacent rings are 21.7° (terminal) and 29.9° (middle). It should be mentioned that in each moiety all three sulfur atoms point in the same direction with short S⋯S separations (S2⋯S3, 3.106(2) Å and S3⋯S4, 3.167(2) Å) in contrast to a conventional all-*anti* conformation, such as that in compound **2** with a shorter chain. The presence of the long-chain structure and *n*-butyl groups is believed to contribute significantly to this array.

An offset layer packing structure is constructed in the crystal packing of **5** in which strong π–π stacking interactions between adjacent thiophene rings are observed. As shown in Figure 4 (top), a shift of about one thiophene ring is found among vicinal molecules forming the offset layer

Figure 3. Perspective view of the packing structure of **2** with the unit cell; hydrogen atoms are omitted for clarity.
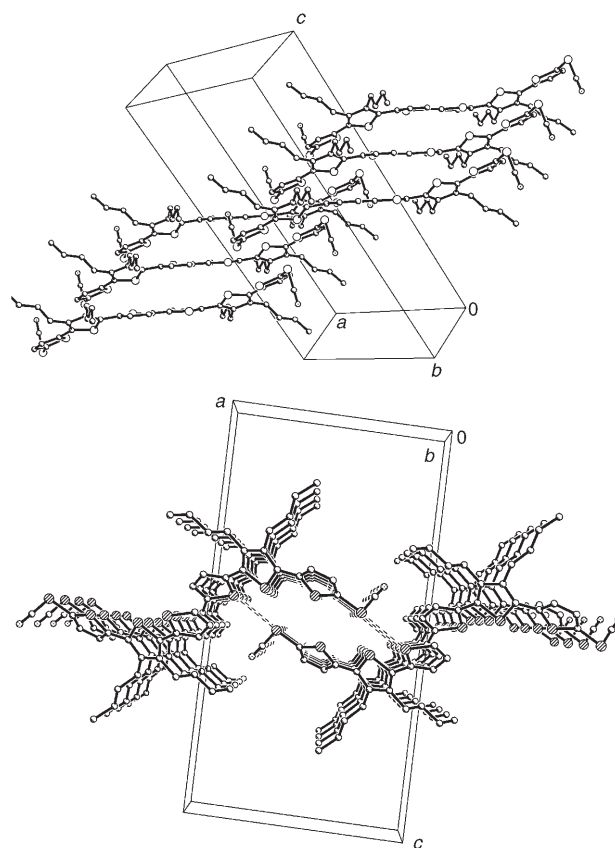

Figure 4. Perspective views of the layer packing structure of **5** parallel (top) and perpendicular (bottom) to the molecular plane together with the unit cell; hydrogen atoms are left out for clarity.

packing. Adjacent middle thiophene rings are parallel with the separation of 3.48 Å, indicative of strong π stacking. Moreover, each terminal thiophene ring bound to the thiocyano groups is found to interact with one neighboring terminal thiophene ring through the offset π–π stacking with the shortest contact of 3.64 Å. In addition, a weak S⋯S contact between SCN and middle thiophene sulfur atoms (S1–S4A ($1-x$, $1-y$, $-z$), 3.418(2) Å) is observed between adjacent molecules, further stabilizing the structure (Figure 4 bottom). In contrast to **5**, no π–π stacking interaction can be observed in **2** because of the existence of strong spatial hindrance of *n*-butyl and thiocyano groups for short chain, as shown in Figure 3. Moreover, neither inter- nor intramolecular hydrogen-bonding interactions are observed in either structure.

To date, there have been several structural reports on oligothiophenes with different numbers of thiophene rings and different substituted groups such as 3′,3′′′′,4′,4′′′′-tetrabutyl-sexithione, 3′,4′-dibutyl-5′5′′-diphenyl-2,2′:5′,2′′-terthiophene, 4′′,3′′′-dimethyl-2,2′:5′,2′′:5′′,2′′′:5′′′,2′′′′:5′′′′,2′′′′′-sexithiophene, and α,ω-dicyanooligothiophenes NC-$(C_4H_2S)_n$CN ($n=3–6$).[13] Our motivation is to prepare oligothiophenes capped at the ends by dithiol groups that can then bridge Au-NPs. Here thiocyano groups are very stable and can be easily transformed to thiol groups through reduction by LiAlH$_4$. Since it is also the first time for us to introduce terminal thiocyano groups to oligothiophenes, we determined the crystal structures of the representative compounds **2** and **5**. From their single-crystal structures, we know that the distance between the terminal sulfur atoms is 1.36 nm in **2**, and this separation for **5** is 2.16 nm. Furthermore, we can predict the length of **8** is approximately 3.16 nm, which can be estimated by its optimal configuration with the help of quantum chemical calculations. These data will help us to understand their electronic behaviors better and possible mechanism of electronic conduction.

Electronic spectra: The UV-visible spectra of **2**, **5**, and **8** in chloroform and in the solid state were measured and the maximum absorptions were analogous to those reported oligothiophenes.[14] Bathochromic shifts were observed for both of them because this π–π* transition of thiophene rings is known to be shifted to lower energies when the number of thiophene rings is increased.[15, 12a] In comparison with the absorptions in solution, lower energy absorptions and larger red shifts were observed for the crystalline solids, which is a

reflection of their solid structures. As mentioned above, compound **5** has much better conjugated π system than **2** and stronger π–π stacking interactions are present between molecules in its packing structure. Consequently, from **2** to **5**, red shifts of 86 and 58 nm in solid and in solution were recorded, respectively. In comparison with **5**, compound **8** has only a slightly better delocalized π system; hence red shifts of only 7 and 14 nm in solid and in solution were obtained on going from **5** to **8**, respectively. In this case, the influence of changing the terminal group from SCN to SH is not so evident compared with the main structure, thus similar electronic spectra were recorded with red shifts of 49 and 5 nm on going from **9** to **10** and from **10** to **11**, respectively (see Supporting Information).

Characterization of the self-assembled films: SEM and AFM studies provide further insight into the morphologies of these self-assembled films between the 1 μm gap Au-electrodes. Figure 5 shows SEM images of the molecular junc-
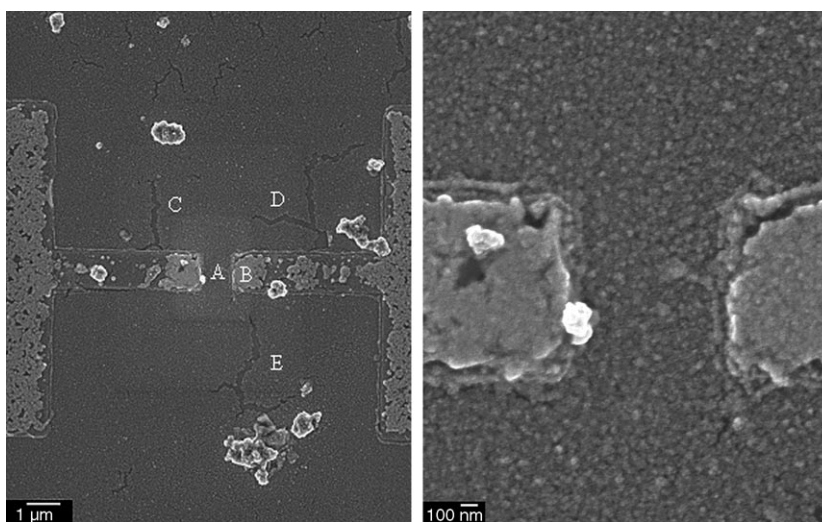

Figure 5. SEM images of the self-assembled film of **14** on the 1×1 μm^2 micro-gap gold electrodes with different magnifications.

tion **14** on the electrodes, in which the self-assembled film covers a wide region around the Au electrode pair. These images clearly manifest the formation of the self-assembled film between the micro-gap Au-electrodes. AFM determinations on the same film uncover the detailed information on the aggregation of the particles, thickness of the film, and distance-dependent *I–V* behavior between the micro-gap Au-electrodes. Figure 6 (top left) is the tapping mode AFM (TM-AFM) morphology of the area **A** (1×1 μm^2) marked in Figure 5 (left), over which the height of film varies only within 10 nm. In view of the average size of Au-NPs (3.3 ± 1.0 nm) and the molecular length of dithiol **11** (3.16 nm) in this case, the size of one isolated gold nanoparticle can reach 10 nm; this value is in agreement with the height variation observed in the AFM images. Similar morphologies can be observed from the AFM images for the films of **12**
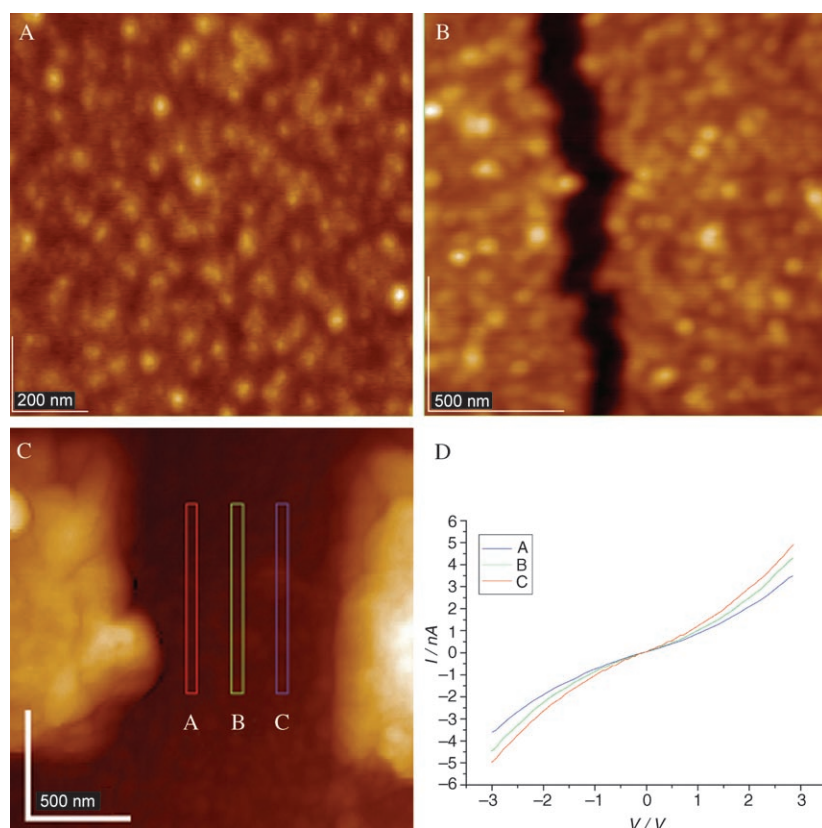
Figure 6. Top: TM-AFM topographies of the self-assembled film of **14** on the micro-gap gold electrodes; A and B correspond to the areas marked in Figure 5 (left). Bottom: C) topographic image of the electrode, and D) I–V curves with different separations between cantilever and brass substrate by using CM-AFM.

Current–voltage characteristics of self-assembled films for 12, 13, and 14: The devices prepared in this paper are very stable in air, although oligothiophenes end-capped by thiols are easily oxidized, and they remain unchanged over a large range of voltage under repeated cycling (−16 to +16 V). In our experiment, the I–V curves (measured current versus voltage) were recorded from −4 to 4 V with 0.05 V intervals by using a cyclic scanning method. All the I–V curves are almost linear in this range. If a higher concentration is employed (prepared from 0.5 mol L^{-1} solutions), a thicker film containing more gold atoms and bridging dithiols is formed. As a result, higher values of current could be recorded. However, the tunneling current could also be observed at low temperature in this case.

The I–V curves of one typical junction of **12** are shown in Figure 7 (top left); they are linear over a wide range of temperature (6–300 K). The maximal current at −4 V and 300 K reaches 475 nA. As seen in Figure 7 (top right), the Arrhenius plots (ln(T) versus 1/T) can be used to characterize the I–V behaviors of this device, from which two types of mechanisms can be found. At low temperature (6–40 K), the currents are temperature independent, since in this range the conductance is governed by only the tunneling between Au-NPs in 1×1 μm^2 region. From 40 to 160 K, the tunneling current and the thermal excitation current (thermally excited electrons hop from one isolated state to the next, the conductance of which depends strongly on the temperature) co-dominate the I–V behavior, since they are comparable during this stage (Figure 7 bottom left). However, when the temperature increases from 160 to 300 K, thermal excitation dominates the conduction behavior. Linear fits for linear parts of eight curves (160–300 K) at different voltages (0.5–4.0 V) give mean value of the activation energy $\Delta E = 0.0073$ eV for **12** (Figure 7 bottom right). Similar I–V characteristics were observed for the thick molecular junctions of **13** and **14**, and mean values of the activation barriers for hopping $\Delta E = 0.016$ eV for **13** and $\Delta E = 0.041$ eV for **14**, respectively, were obtained by using the same method.

and **13**, which mean all the self-assembled films prepared in this paper can cover a large zone including the micro-gap Au-electrodes with uniform morphologies.

The presence of the cracks in the film makes the thickness determination possible. TM-AFM images corresponding to the areas **C**, **D**, and **E** (marked in Figure 5 left) in the 1–3 μm^2 range exhibit similar thickness distributions of the films at 18–24 nm, at which 3–4 layers dithiol bridged Au-NPs are supposed to be present (images of areas **B**, **D**, and **E** are included in Supporting Information). Conductive mode AFM (CM-AFM) scanning gives the distance-dependent I–V characteristics of the film, for which one Au-electrode (the left one in Figure 6 bottom) is connected to the brass substrate by means of a gold wire and a conductive cantilever serves as the other electrode. The plots of average current at different regions marked as **A**, **B**, and **C** within the pair of micro-gap electrodes versus applied bias voltage give three symmetric I–V curves in the voltage range −3–3 V. As shown in Figure 6 (bottom), the current is of the order of nanoamperes, but decreases when the distances between two working electrodes increases; these results provide evidence for the semiconductor properties for this film. All the above-mentioned results prompted us to explore further the electronic characteristics of these devices.

For the thin films (prepared from 0.1 mol L^{-1} solutions), almost no current (less than 1×10^{-13} A) was recorded at low temperature (< 40 K). Nevertheless, stable I–V curves are
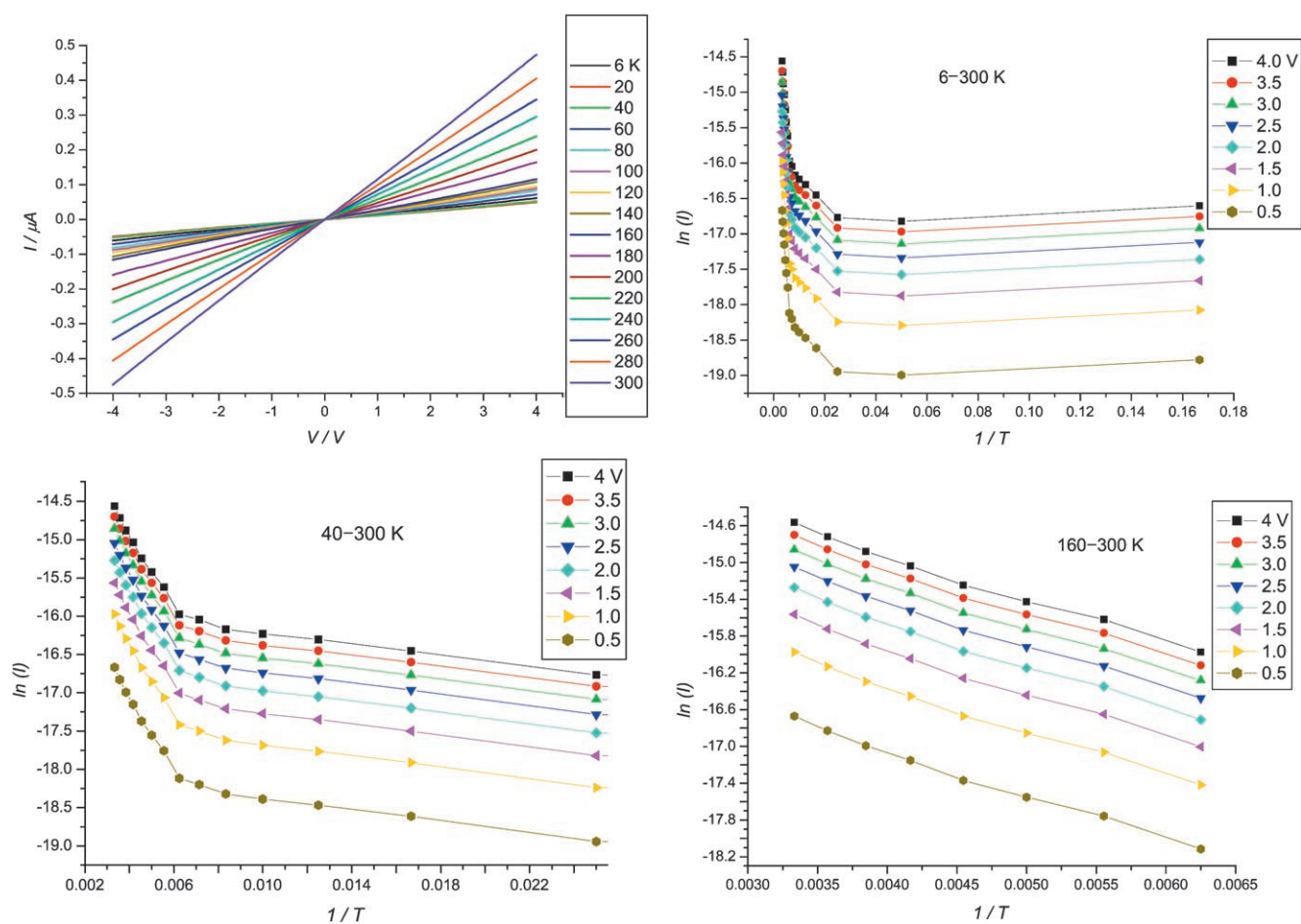
Figure 7. *I–V* characteristics of the molecular junction **12** with thick film. Top left: full range of the *I–V* curves (6–300 K) for a typical device. Top right and bottom left and right: the Arrhenius plots at 0.5–4 V in different temperature regions.

obtained when the temperature exceeds 60 K. As seen in Figure 8 (top), the *I–V* curves of thin film **13** in the temperature range 60–300 K with 20 °C intervals show smooth and reproducible, linear temperature-dependent characteristics for this device. Figure 8 (middle) shows the experimental points of currents at different voltages ranging from 0.5 to 4 V at 0.5 V intervals, from which one can see the current increases significantly to approximately 20 nA when the temperature increases to 300 K. As illustrated in Figure 8 (bottom), the Arrhenius plots at different voltages (0.5–4.0 V) exhibit good linearity in the temperature range 60–300 K, which mean the semiconductor characteristics of this molecular junction are governed by thermal conduction mechanism. Subsequent linear fits for eight curves give the mean value of activation energy $\Delta E = 0.050$ eV.

Different from bulk materials in which the electronic conduction is dominated by intermolecular or interdomain interactions, the predominant mechanism of electronic conduction for the individual molecules is tunneling when the Fermi level of the electrode does not match with the molecular orbital levels at which a contact barrier is formed.[16] The most prevalent theories for metal–molecule systems are thermionic emission, direct tunneling, and defect-mediated transport, such as hopping.[3] Selzer et al. have newly reported the quantitative comparison of two types of junctions with the same molecule; one based on an isolated individual molecule and the other on a SAM.[17] In their SAM junction with ~100 meV activation energy at 0.1 V, two possible electron-transport mechanisms of heat dissipation were proposed: 1) local heating is attributed to electrons or holes dissipating energy as they fall down the potential slope when traversing the molecule, and 2) an inelastic electron-tunneling processes in the off-resonance regime can also store heat in a molecule by exciting various vibration modes.[18]

In this paper, the sizes of three dithiols are far smaller than the electrode gap; thereby two large-area Au-electrodes can only be covalently connected by organic molecules in large quantity by the assistance of the Au-NPs. These three-dimensional nanostructures show similar *I–V* characteristics and barriers to injection (ΔE) to the SAM junction. Hence similar theories can be used to explain the conduction mechanisms. Since both Fower–Nordheim tunneling and direct-tunneling processes do not depend on the temperature (to first order), but strongly depend on the film thickness and voltage,[3] the thickness of the film is relatively important especially for the conduction mechanisms at low
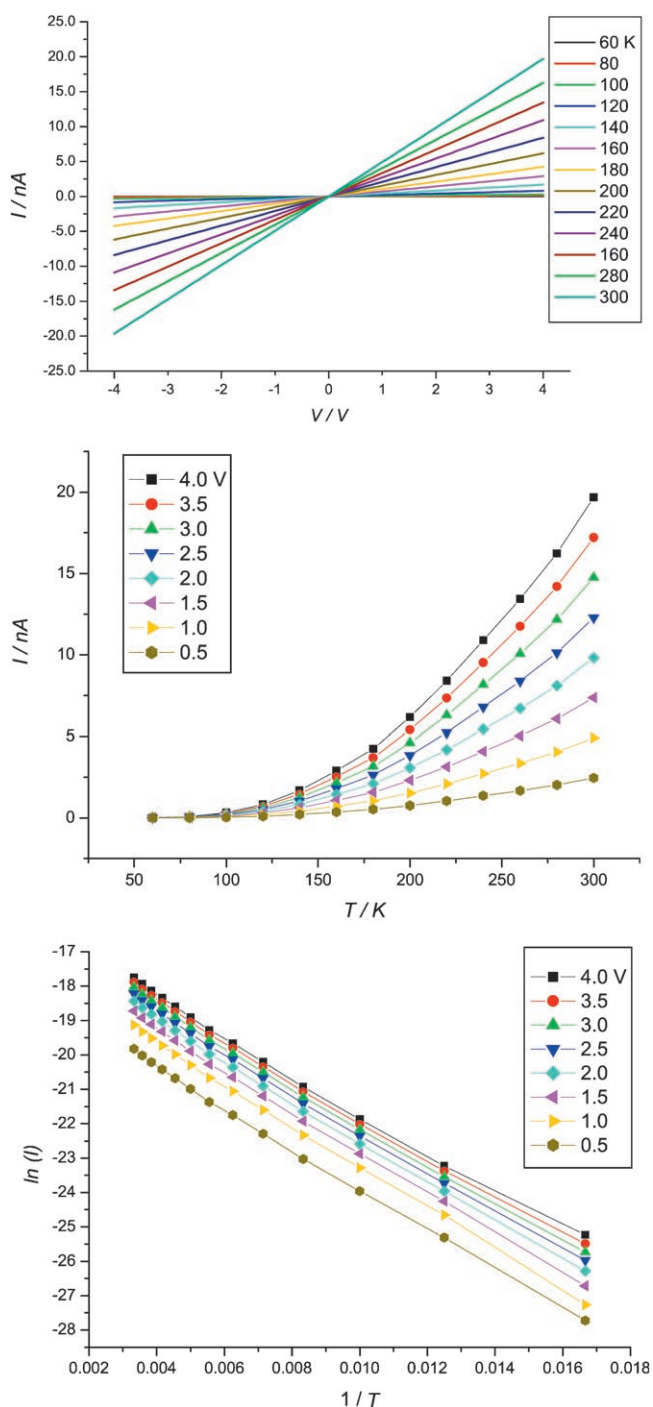
Figure 8. *I–V* characteristics of molecular junction **13** with thin film. Top: Full range of the *I–V* curves (60–300 K) for a typical device. Middle: *I–T* curves in the bias voltage range of 0.5–4 V. Bottom: Classical Arrhenius plots at 0.5–4 V with 0.5 V intervals in different temperature regions.

temperature. That is why the contribution of tunneling current can only be observed for thick films at low temperature in our case. However, at high temperature, thermal effects will dominate the conduction because the activation barriers for hopping are relatively small (< 50 meV), and more and more resonance transmission channels will open for electrons. Moreover, the current excited in this way is much stronger than the temperature-independent tunneling current and it will cover the contribution of the latter. As a consequence, we can explain the temperature-dependent *I–V* behavior at higher temperature for all the devices. In fact, all the devices have similar *I–V* characteristics at high temperature. However, thicker films, which contain more Au-NPs and dithiols, may decrease the energy barriers of our molecular junctions a little. It should be noted that conduction mechanism is also affected by the interactions of the electrodes with the individual molecules; this is the basic conception in molecular electronics. Thus similar but different *I–V* behaviors and ΔE values for these above-mentioned films can be obtained corresponding to the molecules with different lengths.

Preliminary research for photoresponse properties of self-assembled films for 12, 13, and 14: The *I–V* curves of the photoresponse for **12**, **13**, and **14** were measured at 80, 160, 300 K (10 minutes after the metal halide lamp gave the maximal power), and those that were not exposed to the lamp also collected for comparison. A time–current scan mode with 0.3 s intervals was used at -3 V potential to record the process of the photoresponse, and the light source was switched periodically. When the strong light was irradiated to the devices, the surface temperature of the devices increased slightly at first and then decreased with control of the thermostat, but the range only varied within 0.5 K. All the experiments were carried out at midnight in order to prevent the influence of the surrounding light.

As clearly seen in Figure 9 (top), the linear *I–V* curve of **12** under irradiation (red) is increased compared with that measured in the dark (black); this means that the photoresponse in this case is voltage independent. The linear fits of two *I–V* graphs give the ratio of 2.00 ($K_{\text{light}}/K_{\text{dark}}$), which suggests that the photoresponse can double the conductance of this device. However, the rates of conductance are strongly influenced by the temperature. In our experiments, this value decreases to 1.23 at 160 K and 1.02 at 300 K for **12** (Figure 9 middle and bottom). Further study hints that the degree of photoresponse will decrease when the molecular length of the oligothiophene-based dithiols increase. For instance, the ratios of conductance for **12**, **13** and **14** at 80 K decrease from 2.00 to 1.41 (Figure 10 top) and 1.32 (Figure 10 bottom). From the plots of time versus current, illustrated in the insets of Figure 9, we can see the photoresponse processes for these devices are reversible and reproducible. However the speed of photoresponse is a function of time that can be divided into two parts. Repeated on–off cycles of illumination show that a rapid process takes place first and then a relatively slow process (more than 50 s) increasing the current to the maximum when the light is turned on or decreasing it to the minimum when the light is turned off. This behavior is different from the self-assembled porphyrin nanorods for which the photoconductivity grows over hundreds of seconds with light exposure and decays slowly when the light is off.[19] It is also different from the self-assembled Au-S-C$_{60}$ system in toluene on optically
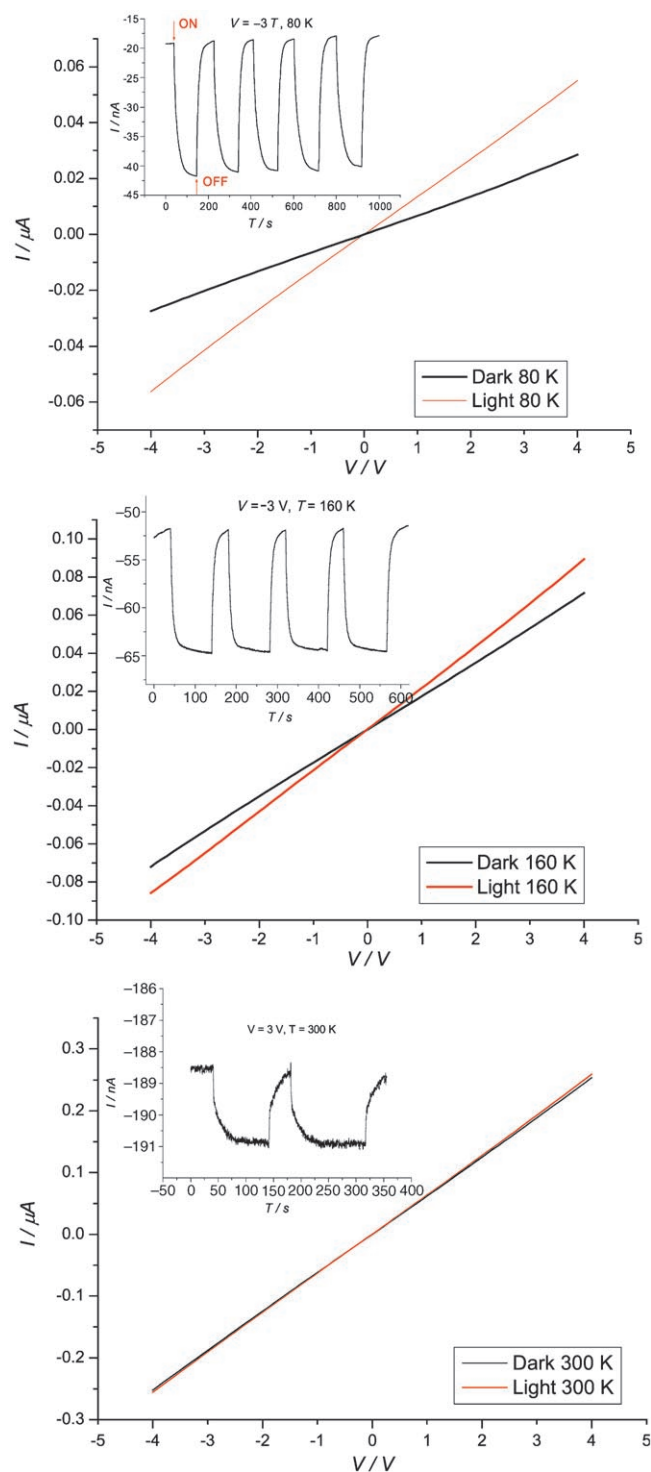
FULL PAPER

Figure 9. Reversible photoresponsive *I–V* and *I–T* curves of device **12**. Top: *I–V* curves under irradiation (red one) and in dark conditions (black one) in the range −4 to +4 V at 80 K. The inset is *I–T* curve when the light is turned on or off periodically at −3 V, 80 K. Middle and bottom: *I–V* curves under irradiation (red) and in the dark (black) in the range −4 to +4 V at 160 and 300 K, respectively. The insets are *I–T* curves when the light is turned on or off periodically at −3 V, 160 K and 300 K, respectively.
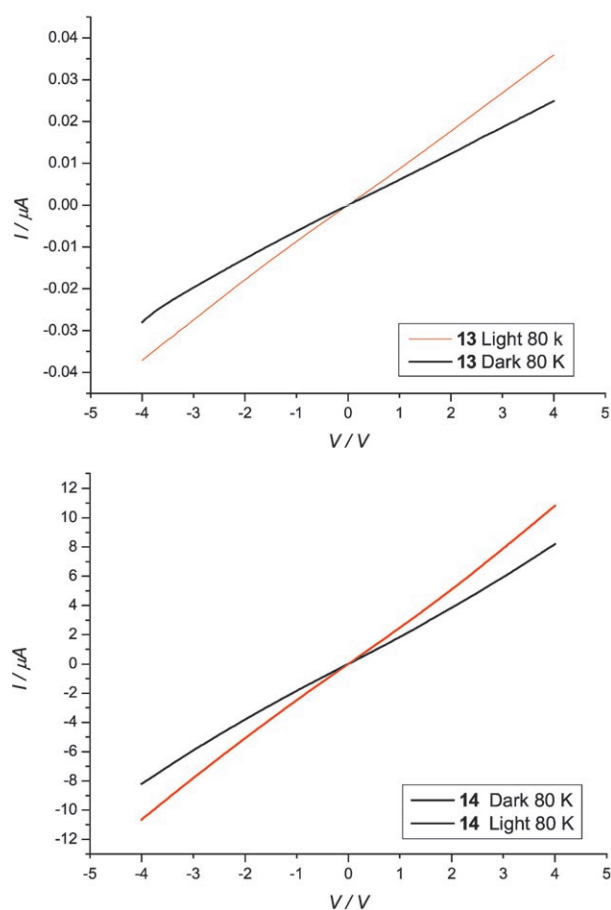

Figure 10. Photoresponsive *I–V* curves (red ones) of **13** (top) and **14** (bottom) at 80 K compared those in dark condition (black ones).

transparent electrodes for which prompt photoresponsive behavior was observed.[20]

Before discussing the possible mechanism of photocurrent generation in the on–off cycles of illumination, we should exclude the possibility of thermal effects on the generation of current, because the light source we used has a wide range of wavelength. From the experimental results we have obtained, we can ignore these effects by using the effective thermostat (±0.5°) and the reference experiments at every temperature. For the reference experiments, we prepared films composed of substituted phenylethynylbenzene-based dithiols with different chain lengths and the same active Au-NPs under similar conditions, but no photoresponse was observed at either low or room temperature.

Two distinctively different mechanisms, namely photogalvanic and photosensitization processes, can be operative in the anodic photocurrent generation.[21] In our mode, Au-NPs have the unique ability to store electrons[22] and promote the charge separation and facilitate electron transportation[23] within the film during the photocurrent process. Furthermore, the robust coverage and high surface area of the nanostructured film play a key role in this process. On the other hand, the selection of thiol molecules to combine with Au-NPs is very important, because it will have a significant

influence on the electron energy levels of the combined metal–molecule system. Molecules with a good delocalized conjugated π system, such as porphyrin and oligothiophene, and suitable functionized groups, such as thiol and thiol ether, will be good candidates so that small activation barriers for hopping can be obtained. When electrons are photoexcited from the HOMOs to the LUMOs, if the LUMOs are closely coupled (which can be achieved by using suitable molecules), transport through the LUMOs and HOMOs other than the relaxation from LUMOs back to the HOMOs will be favored. Here temperature is also a factor that should be taken into account, since it can influence the HOMO–LUMO gap energy for a given device. Besides the aforementioned physical factors, some photochemical processes are believed to occur in this process, because the *I–T* curves of our devices show relatively slow photoresponses (the second part). The irradiation appears to give rise to some electron carriers and these photochemically generated carriers can further increase the current between the junctions, and vice versa. As the photochemical process is much slower than the physical process, time-dependent increase and decrease of the current can be observed for all junctions when the light is switched on and off periodically.

There have been several reports about the photoresponse of some silicon-based semiconductor devices and organic compounds.[24–25] However, as far as we are aware, this is the first report about the photoresponsive compounds in which an Au-NP-containing self-assembled film is involved in the solid state. In fact, photoresponse is a very interesting phenomenon and it has many future opportunities for designing photovoltaic cells, photoswitchable molecular-based devices, and photomodulated sensors. As very stable and easily prepared devices can be obtained by self-assembly method in our case, this sort of research deserves more attention and it is expected to have utility in molecular electronics.

Conclusion

In this paper, we described the synthesis and characterization of three oligothiophene-based terminal dithiols with different molecular lengths (1.36, 2.16, and 3.16 nm) and their self-assembled films with active Au-NPs (3.3±1.0 nm) by using ligand-exchange and binding between microgap gold electrodes. UV-visible spectra of these compounds in solution and in the solid state show different red shifts, which are related to the different packing modes in the single-crystal structures. SEM and AFM morphologies for one typical device reveal further information on the morphologies of these self-assembled films; the height variation of the well-oriented film is less than 10 nm (corresponding to the size of isolated Au-NPs) and the thickness of 18–24 nm suggests the formation of 3–4 layers dithiol-bridged Au-NPs. Distance-dependent *I–V* characteristics of the film were also probed by using conductive AFM technologies. Temperature-dependent *I–V* curves of these devices with different thickness and molecular lengths in the range 6–300 K were discussed,

and an explanation for the possible conduction mechanism was also included. Classical Arrhenius plots were further applied to calculate the activation energies for different metal–film–metal junctions. More importantly, preliminary reversible photoresponsive properties for the aforementioned devices at different temperatures are discussed and the magnitude of the current can reach twice that recorded in dark at 80 K for the experimental bias voltage range −4 to +4 V. Some physical and photochemical mechanisms dominate the photoresponsive processes. Further studies on this type of molecular junctions such as wavelength dependence for the photoresponse properties and some Ru^{II} coordination complexes bearing 3,8-disubstituted 1,10-phenanthroline ligand with high photoresponse are now being undertaken.

Experimental Section

Materials and measurements: All reagents and solvents were of analytical grade and used without further purification. The anhydrous solvents were drawn up into a syringe under a flow of dry N$_2$ gas and were directly transferred into the reaction flask to avoid contamination. The nomenclature used in the drawings is related to molecular symmetry and does not correspond to the IUPAC nomenclature used in the Experimental Section. The intermediates and products were characterized by elemental analysis and spectroscopic methods. 2-Dodecanethiol-protected active Au-NPs were prepared by the modification of the Brust method.[26]

The UV-visible spectra were recorded with a Shimadzu UV-3150 double-beam spectrophotometer. The IR spectra were recorded in a Horiba FT-700 spectrophotometer. ^{1}H NMR spectra were collected on a Varian Unit 500 MHz spectrometer and a JEOL GSX 270 MHz spectrometer. ^{13}C NMR data were obtained at 67.8 MHz with a JEOL GSX spectrometer. The DI-EI (70 eV) mass spectra were given by a Hitachi M80-B spectrometer. FAB-MS and TOF-MS spectra were measured with a JEOL JMS-777 V spectrometer. Scanning electron microscope (SEM) images were collected with a JEOL JSM-6700F microscope with the acceleration voltage at 3 kV. An OLYMPUS BX60 M optical microscope was used to check all the electrodes before the determination of the *I–V* curves. A Yanaco PLASMA ASHER LTA-102 instrument was used to clean all the electrodes. The light source used for irradiating the samples with the maximal intensity is a NPI PCS-UMX250 high-power metal halide lamp. Atomic force microscope (AFM) images were recorded on a JEOL-JSPM4210 instrument. The measurement was carried out in vacuum to eliminate the influence of water adsorbed on the sample surface and increase the sensitivity and reproducibility of the experiment. The resonant frequency of the cantilevers was 250 kHz for tapping mode. Contact-mode AFM was used to measure the *I–V* curve in which Pt-coated conductive cantilevers were used to measure current.

The gold nanoelectrodes with 1 μm gaps were prepared as follows. Successive layers of Ti, Au, and electron beam resist polymer were deposited on a four inch *n*-doped silicon wafer, covered by a 200 nm layer of thermally grown SiO$_2$. It was patterned by conventional electron beam lithography and the exposed metal was removed with Ar$^+$ beams to define the nanogap electrodes. It was then covered with a 100 nm thick Si$_3$N$_4$ layer after stripping out the resist polymer and the pads and nanogaps were open by conventional electron beam lithography as mentioned above. Each 3×3 mm silicon chip was thoroughly washed with toluene, acetone, and methanol and cleaned in an oxygen plasma asher before SEM analysis. As for the preparation for the self-assembled films with 2-dodecanethiol-protected active Au-NPs in CHCl$_3$, the electrodes with 1 μm gaps were cleaned carefully by CF$_4$ plasma and checked by the microscopy before use.

FULL PAPER

The *I–V* curves were collected by an Advantest R6245 2Channels voltage–current source monitor interfaced to a microcomputer through a GPIB-SCSI board and NI-488.2 protocol. The data were acquired with a homemade procedure and IgorPro 4.0 (Wavemetrics) software. The samples were mounted on the top of an anti-vibration table with a temperature-controlled cryogenic chamber ($\pm$ 0.005 °C). All measurements were carried out in high vacuum (P $<$ 2.0 × 10^{-4} Pascal) by means of the turbo pump, and the samples were cooled by using liquid helium as coolant (6 to 300 K). Triaxial cables were used to connect the molecular devices and the *I–V* monitor in order to minimize the external noise.

X-ray data collection and refinement: Single-crystal samples of **2** and **5** were covered in glue and mounted on a glass fiber and used for data collection on a Rigaku Mercury CCD area-detector at 100(2) K using graphite monochromated Mo$_{K\alpha}$ radiation (λ = 0.71073 Å). The collected diffraction data were reduced by using the program Crystalclear[27] and empirical absorption corrections were done. The original data files generated by Crystalclear were transformed to SHELXTL97 format by the Texsan program,[28] and then the structures were solved by direct methods and refined by least-squares method on F_o^2 by using the SHELXTL-PC software package.[29] All non-hydrogen atoms were anisotropically refined and all hydrogen atoms were inserted in the calculated positions assigned fixed isotropic thermal parameters and allowed to ride on their respective parent atoms. All calculations and molecular graphics were carried out with the SHELXTL PC program package on a PC computer. The summary of the crystal data, experimental details and refinement results for **2** and **5** is listed in Table 1, while selected bond lengths and bond angles for **5** are given in Table 2.

Table 1. Crystal and refinement data for **2** and **5**.

	2	**5**
formula	$C_{22}H_{22}N_2S_5$	$C_{42}H_{44}N_2S_8$
M_r	474.77	833.27
crystal size [mm]	0.10 × 0.10 × 0.20	0.10 × 0.10 × 0.40
crystal system	monoclinic	monoclinic
space group	Cc (No. 9)	$P2_1/c$ (No. 14)
a [Å]	8.5419(17)	14.151(3)
b [Å]	20.333(4)	5.4799(11)
c [Å]	26.445(5)	26.475(5)
β [°]	95.28(3)	91.04(3)
V [Å^3]	4573.5(16)	2052.7(7)
Z	8	2
ρ_{calcd} [Mg m^{-3}]	1.379	1.348
μ (Mo$_{K\alpha}$) [mm^{-1}]	0.519	0.468
$F(000)$	1984	876
max/min transmission	0.903/0.950	0.835/0.955
Flack parameter	0.07(19)	–
parameters	491	237
$R1/wR2$ $[I > 2\sigma(I)]^{[a]}$	0.0952/0.2416	0.0951/0.1645
$R1$, $wR2$ (all data)$^{[a]}$	0.0974/0.2427	0.1135/0.1717
goodness of fit (S)	1.151	1.106
Δ [e Å^{-3}] (max/min)	0.918/−0.848	0.352/−0.336

[a] $R1 = \Sigma ||F_o| - |F_c|| / \Sigma |F_o|$, $wR2 = [\Sigma[w(F_o^2 - F_c^2)^2]/\Sigma w(F_o^2)^2]^{1/2}$.

Table 2. Selected bond lengths [Å] and angles [°] for **5**.

Bond lengths		Bond angles	
S1−C1	1.708(8)	C1-S1-C2	98.8(3)
S1−C2	1.768(6)	C2-S2-C5	91.3(3)
S2−C2	1.716(6)	C6-S3-C9	92.3(3)
S2−C5	1.737(6)	C10-S4-C13	92.6(3)
S3−C6	1.721(6)	S1-C1-N1	177.9(7)
S3−C9	1.728(6)	S1-C2-S2	120.6(3)
S4−C10	1.725(6)	S1-C2-C3	126.9(5)
S4−C13	1.719(6)	S2-C2-C3	112.5(4)
N1−C1	1.142(11)		

CCDC-272762 and CCDC-272763 contain the supplementary crystallographic data for this paper. These data can be obtained free of charge from the Cambridge Crystallographic Data Centre via www.ccdc.cam.ac.uk/data_request/cif.

Terthiophenes 1 and 3: Compounds **1** and **3** were prepared by means of the method we have described previously.[11]

Terthiophene 2: A solution of compound **1** (3.6 g, 10.0 mmol) in CHCl$_3$ (20 mL) was added dropwise to a mixture of KSCN (40.1 g, 412.6 mmol) in methanol (100 mL) and Br$_2$ (10.3 mL, ρ = 3.12 g cm^{-3}, 201.1 mmol) in CHCl$_3$ (50 mL) at −78 °C. This mixture was stirred for 4 h at room temperature, quenched with water, extracted with CHCl$_3$, and dried over anhydrous Na$_2$SO$_4$. The solvent was removed by a rotatory evaporator, and the residue was purified by silica-gel column chromatography (*n*-hexane). A yellow crystalline product was obtained (yield: 89.1 %) after recrystallization from CHCl$_3$/*n*-hexane. M.p. 87–88 °C; ^{1}H NMR (270 MHz, CDCl$_3$, 25 °C, TMS): δ = 7.39 (d, J = 3.9 Hz, 2H), 7.10 (d, J = 3.9 Hz, 2H), 2.70 (t, J = 8.1 Hz, 4H), 1.58–1.44 (m, 8H), 0.97 ppm (t, 7.1 Hz, 6H); ^{13}C NMR (68 MHz, CDCl$_3$, 25 °C, TMS): δ = 143.94, 141.85, 138.02, 129.59, 126.83, 117.52, 110.09, 32.77, 27.82, 22.90, 13.77 ppm; FT-IR (KBr pellets): $\tilde{v}$ = 2952 (s), 2868 (s), 2154 (s), 1464 (s), 1417 (m), 793 cm^{-1} (s); elemental analysis calcd (%) for $C_{22}H_{22}N_2S_5$: C 55.66, H 4.67, N 5.90; found: C 55.38, H 4.66, N 6.00; UV/Vis (CHCl$_3$): λ_{max} = 359 nm (387 nm for solid); MS (DI-EI): *m/z*: 474 [$C_{22}H_{22}N_2S_5$]$^+$. Yellow needlelike single crystals of **2** suitable for X-ray diffraction determination were grown from a mixed solution of acetone and ethanol (2:1) by slow evaporation in air at room temperature.

Sexithiophene 4: A solution of terthiophene **3** (6.17 g, 14.04 mmol) in dry THF (20 mL) was added dropwise into a suspension of zinc (2.76 g, 42.26 mmol), NiCl$_2$ (0.20 g, 1.54 mmol), and PPh$_3$ (2.96 g, 11.29 mmol) in dry THF (30 mL) under an N$_2$ atmosphere at 60 °C. The mixture was then stirred overnight at room temperature, and was then filtered and extracted with CHCl$_3$. The organic layer was washed with water and saturated brine, and dried with anhydrous Na$_2$SO$_4$. The solvent was removed by a rotatory evaporator and the residue was purified by silica-gel column chromatography (*n*-hexane). An orange crystalline product was obtained (yield: 78.0 %) after recrystallization from CHCl$_3$/*n*-hexane. M.p. 117–118 °C; ^{1}H NMR (270 MHz, CDCl$_3$, 25 °C, TMS): δ = 7.31 (d, J = 1.2 Hz, 2H), 7.30 (d, J = 1.2 Hz, 2H), 7.15–7.04 (m, 6H), 2.74–2.68 (m, 8H), 1.54–1.43 (m, 16H), 1.00–0.93 ppm (m, 16H); ^{13}C NMR (68 MHz, CDCl$_3$, 25 °C, TMS): δ = 140.19, 136.68, 136.11, 135.25, 130.00, 129.99, 129.61, 127.36, 126.33, 125.89, 125.35, 123.81, 32.90, 32.84, 27.94, 27.80, 23.03, 22.99 ppm; FT-IR (KBr pellets): $\tilde{v}$ = 2954 (s), 2854 (s), 1496 (m), 1464 cm^{-1} (s); elemental analysis calcd (%) for $C_{40}H_{46}S_6$: C 66.81, H 6.45; found: C 66.62, H 6.39; UV/Vis (CH$_2$Cl$_2$): λ_{max} = 412 nm; MS (DI-EI): *m/z*: 718 [$C_{40}H_{46}S_6$]$^+$.

Sexithiophene 5: A solution of compound **4** (1.33 g, 1.85 mmol) in CHCl$_3$ (15 mL) was added dropwise to a mixture of KSCN (10.9 g, 112.15 mmol) in methanol (30 mL) and Br$_2$ (2.9 mL, ρ = 3.12 g cm^{-3}, 56.62 mmol) in CHCl$_3$ (10 mL) at −78 °C. This mixture was stirred for 4 h at room temperature, quenched with water, extracted with CHCl$_3$, and dried over anhydrous Na$_2$SO$_4$. The solvent was removed by a rotatory evaporator and the residue was purified by silica-gel column chromatography (*n*-hexane). A yellow crystalline product was obtained (yield: 85.6 %) after recrystallization from CHCl$_3$/*n*-hexane. M.p. 174–175 °C; ^{1}H NMR (270 MHz, CDCl$_3$, 25 °C, TMS): δ = 7.39 (d, J = 3.9 Hz, 2H), 7.10 (d, J = 3.9 Hz, 2H), 7.09 (d, J = 3.9 Hz, 2H), 7.08 (d, J = 3.9 Hz, 2H), 2.72–2.68 (m, 8H), 1.56–1.45 (m, 8H), 1.01–0.96 ppm (br, 12H); ^{13}C NMR (68 MHz, CDCl$_3$, 25 °C, TMS): δ = 144.62, 141.82, 140.51, 138.10, 137.01, 134.75, 131.26, 128.23, 126.88, 126.38, 124.07, 110.26, 32.86, 27.92, 22.99, 13.84 ppm; FT-IR (KBr pellets): $\tilde{v}$ = 2954 (s), 2929 (s), 2860 (s), 2156 (m), 1518 (m), 1456 (s), 1435 cm^{-1} (m); elemental analysis calcd (%) for $C_{42}H_{44}N_2S_8$: C 60.53, H 5.32, N 3.36; found: C 60.29, H 5.28, N 3.35; UV/Vis (CHCl$_3$): λ_{max} = 417 nm (473 nm for solid); MS (FAB): *m/z*: 833 [$C_{42}H_{44}N_2S_8$]$^+$. Orange needlelike single crystals of **5** suitable for X-ray diffraction determination were grown from a mixed solution of *n*-hexane and chloroform (1:3) by slow evaporation in air at room temperature.

Terthiophene 6: A solution of NBS (7.88 g, 6.96 mmol) in 50 mL DMF was added dropwise to a solution of terthiophene **1** (7.98 g, 22.1 mmol) in DMF (150 mL) at room temperature. The mixture was stirred overnight, poured into a saturated brine solution (400 mL), and extracted with CHCl$_3$. The organic phase was washed thoroughly with distilled water, saturated brine and distilled water, and then dried over anhydrous Na$_2$SO$_4$. The solvent was removed by a rotatory evaporator and the residue was purified by silica-gel column chromatography (*n*-hexane). A yellow liquid was obtained (yield 56.2%). ^{1}H NMR (270 MHz, CDCl$_3$, 25°C, TMS): $\delta = 7.00$ (d, $J = 1.5$ Hz, 2H), 6.86 (d, $J = 1.5$ Hz, 2H), 2.65 (t, $J = 2.4$ Hz, 4H), 1.54–1.27 (m, 8H), 0.94 ppm (t, 3.6 Hz, 6H); ^{13}C NMR (68 MHz, CDCl$_3$, 25°C, TMS): $\delta = 140.56$, 137.45, 130.19, 129.35, 126.23, 111.97, 32.93, 27.82, 27.79, 13.82 ppm; FT-IR (KBr pellets): $\tilde{v} = 2950$ (s), 1461 (s), 1060 (m), 778 cm^{-1} (s); elemental analysis calcd (%) for C$_{20}$H$_{22}$Br$_2$S$_3$: C 46.34, H 4.28; found: C 46.38, H 4.25; MS (DI-EI): *m/z*: 518 [C$_{20}$H$_{22}$Br$_2$S$_3$]$^+$.

Nonathiophene 7: Magnesium (0.96 g, 40 mmol) was transferred to a three-necked round-bottomed flask and heated to 100°C in the N$_2$ atmosphere. After the mixture was cooled down to room temperature, dry THF (10 mL) and some iodine were added. The mixture was left to react for 10 min under magnetic stirring, and then terthiophene **3** (7.2 mL, 16.2 mmol) in THF (10 mL) was carefully added. The mixture was refluxed for 5 h to obtain the corresponding Grignard reagent. This was slowly added to a solution obtained by dissolving **6** (3.50 g, 8.0 mmol) and [NiCl$_2$(dppp)] (0.15 g, 0.16 mmol) in dry THF (40 mL). The mixture was refluxed for 4 h in the N$_2$ atmosphere. The reaction mixture was stirred for additional 12 h at room temperature, quenched with 1 mol L^{-1} hydrochloric acid, and extracted with CHCl$_3$. The organic phase was washed thoroughly with saturated brine and distilled water, and then dried over anhydrous Na$_2$SO$_4$. The solvent was removed by a rotatory evaporator and the residue was purified by silica-gel column chromatography (30% CHCl$_3$/*n*-hexane). A red powder was obtained in 74.4% yield. M.p. 160–161°C; ^{1}H NMR (270 MHz, CDCl$_3$, 25°C, TMS): $\delta = 7.31$ (d, $J = 1.4$ Hz, 2H), 7.14–7.02 (m, 12H), 2.73–2.69 (m, 12H), 1.54–1.46 (m, 24H), 0.98–0.92 ppm (m, 18H); ^{13}C NMR (68 MHz, CDCl$_3$, 25°C, TMS): $\delta = 140.35$, 140.19, 140.17, 136.78, 136.11, 135.31, 135.14, 130.03, 129.80, 127.36, 126.40, 126.35, 125.89, 125.36, 123.84, 32.92, 32.88, 32.80, 27.98, 27.92, 27.79, 23.05, 23.02, 22.98, 13.88, 13.84 ppm; FT-IR (KBr pellets): $\tilde{v} = 2954$ (s), 1457 (m), 786 (s), 686 cm^{-1} (m) cm^{-1}; elemental analysis calcd (%) for C$_{60}$H$_{68}$S$_9$: C 66.86, H 6.36; found: C 66.80, H 6.33; MS (TOF-MS): *m/z*: 1079 [C$_{60}$H$_{69}$S$_9$]$^+$.

Nonathiophene 8: The synthetic procedure for the preparation of **8** is analogous to those of **2** and **5**. A solution of compound **7** (0.30 g, 0.70 mmol) in CHCl$_3$ (10 mL) was added dropwise to a mixture of KSCN (0.068 g, 112.15 mmol) in methanol (3 mL) and Br$_2$ (0.4 mL, $\rho = 3.12$ g cm^{-3}, 7.81 mmol) in CHCl$_3$ (10 mL) at −78°C. This mixture was stirred for 4 h at room temperature, quenched with water, extracted with CHCl$_3$, and dried over anhydrous Na$_2$SO$_4$. The solvent was removed by a rotatory evaporator and the residue was purified by silica-gel column chromatography (60% CHCl$_3$/*n*-hexane). A red crystalline product was obtained (yield: 72.3%) after recrystallization from CHCl$_3$/*n*-hexane. M.p. 152–153°C; ^{1}H NMR (270 MHz, CDCl$_3$, 25°C, TMS): $\delta = 7.38$ (d, $J = 1.4$ Hz, 2H), 7.15 (m, 4H), 7.08 (m, 6H), 2.74–2.72 (m, 12H), 1.54–1.49 (m, 24H), 1.01–0.96 ppm (m, 18H); ^{13}C NMR (68 MHz, CDCl$_3$, 25°C, TMS): $\delta = 144.63$, 141.77, 140.41, 138.09, 136.51, 135.51, 135.25, 134.51, 131.33, 129.97, 128.14, 126.83, 126.40, 126.31, 124.03, 123.87, 116.63, 110.27, 32.82, 27.85, 23.04, 13.87 ppm; FT-IR (KBr pellets): $\tilde{v} =$

2927 (s), 2156 (m), 1457 (s), 1072 (m), 786 cm^{-1} (s); elemental analysis calcd (%) for C$_{62}$H$_{66}$N$_2$S$_{11}$: C 62.48, H 5.58, N 2.35; found: C 62.39, H 5.56, N 2.35; UV/Vis (CHCl$_3$): $\lambda_{max} = 431$ nm (480 nm for solid); MS (TOF-MS): *m/z*: 1192 [C$_{62}$H$_{66}$N$_2$S$_{11}$]$^+$.

Dithiols 9, 10, 11: Compounds **9**, **10**, and **11** were all prepared by a similar method. A suspension of LiAlH$_4$ (0.05 g, 1.3 mmol) in dry THF (10 mL) in the N$_2$ atmosphere in a three-necked round-bottomed flask equipped with a condenser was added carefully the solutions of **2** (0.21 g, 0.50 mmol), **5** (0.10 g, 0.12 mmol), or **8** (0.01 g, 0.0084 mmol), respectively, in dry THF (10 mL) at room temperature. The mixture was then stirred for 2 h and quenched with hydrochloric acid (1 mol L^{-1}). It was then poured into chloroform (50 mL), and washed thoroughly with distilled water and dried with anhydrous Na$_2$SO$_4$. The solvent was removed by a rotatory evaporator and the residues were dried in a vacuum.

Compound 9: Yellow powder (yield: 96.7%); ^{1}H NMR (500 MHz, CDCl$_3$, 25°C, TMS): $\delta = 7.04$ (d, $J = 1.5$ Hz, 2H), 6.94 (d, $J = 1.5$ Hz, 2H), 3.59 (s, 2H), 2.67 (t, $J = 3.0$ Hz, 4H), 1.55–1.38 (m, 8H), 0.95 ppm (t, $J = 2.5$ Hz, 6H); ^{13}C NMR (68 MHz, CDCl$_3$, 25°C, TMS): $\delta = 140.37$, 139.38, 134.33, 129.61, 126.16, 124.41, 32.87, 27.80, 22.97, 13.83 ppm; FT-IR (KBr pellets): $\tilde{v} = 2931$ (s), 2514 (m), 1456 cm^{-1} (m); UV/Vis (CHCl$_3$): $\lambda_{max} = 366$ nm; MS (TOF-MS): *m/z*: 424 [C$_{20}$H$_{24}$S$_5$]$^+$.

Compound 10: Orange powder (yield: 94.3%); ^{1}H NMR (500 MHz, CDCl$_3$, 25°C, TMS): $\delta = 7.13$ (d, $J = 1.5$ Hz, 2H), 7.05 (d, $J = 1.5$ Hz, 2H), 7.04 (d, $J = 1.5$ Hz, 2H), 6.97 (d, $J = 1.5$ Hz, 2H), 3.59 (s, 2H), 2.75–2.65 (m, 8H), 1.56–1.45 (m, 16H), 1.00–0.93 ppm (m, 12H); ^{13}C NMR (68 MHz, CDCl$_3$, 25°C, TMS): $\delta = 140.48$, 140.25, 135.08, 134.37, 129.93, 129.47, 126.47, 126.01, 123.88, 32.87, 27.83, 22.97, 13.87 ppm; FT-IR (KBr
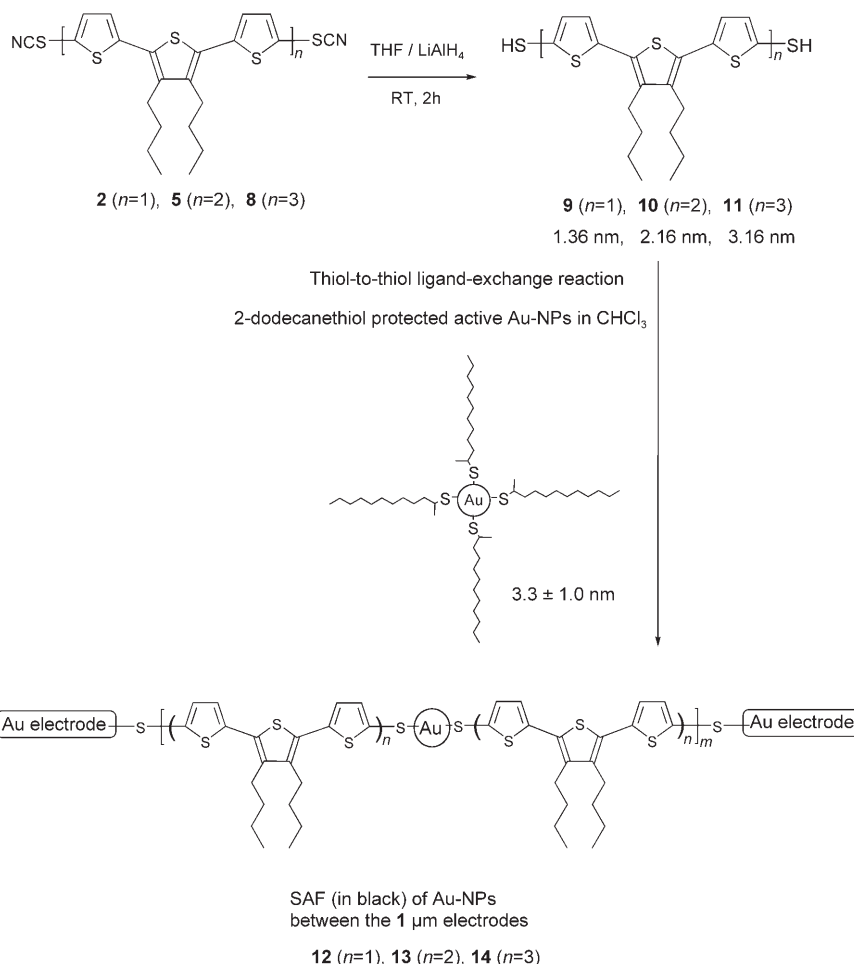
Scheme 2. Schematic illustration of the preparation for the self-assembled films of **12**, **13** and **14**.

pellets): $\tilde{v} = 2950$ (s), 2510 (m), 1455 cm^{-1} (m); UV/Vis (CHCl$_3$): $\lambda_{max} = 415$ nm; MS (TOF-MS): m/z: 782 [C$_{40}$H$_{46}$S$_8$]$^+$.

Compound 11: Red powder (yield: 93.8%); ^{1}H NMR (500 MHz, CDCl$_3$, 25°C, TMS): $\delta = 7.15$ (d, $J = 1.5$ Hz, 2H), 7.06 (m, 4H), 7.01 (m, 6H), 3.58 (s, 2H), 2.74–2.67 (m, 12H), 1.55–1.49 (m, 24H), 1.00–0.95 ppm (m, 18H); FT-IR (KBr pellets): $\tilde{v} = 2945$ (s), 2510 (m), 1454 cm^{-1} (m); UV/Vis (CHCl$_3$): $\lambda_{max} = 420$ nm; MS (TOF-MS): m/z: 1141 [C$_{60}$H$_{68}$S$_{11}$]$^+$.

Preparation of self-assembled films of 12, 13, and 14 in 1×1 μm^2 area: Two concentrations were used to prepare films with different thickness. The junctions were fabricated by the self-assembly method as illustrated in Scheme 2. The freshly cleaned gold electrodes with 1 μm gap 1 μm width were soaked into solutions of **9**, **10**, and **11** (0.1 or 0.5 mmol L^{-1}) in chloroform, respectively, for 30 minutes and then a solution of 2-dodeca-nethiol-protected active Au-NPs (0.1 or 0.5 mmol L^{-1}) in chloroform was added. The mixtures were kept standing for 30 h at room temperature in a glove box, then the electrodes were taken out, washed thoroughly with chloroform in order to remove excess unreacted Au-NPs and dithiols, and dried in vacuum.

Acknowledgements

[1] J. Roncali, *Chem. Rev.* **1997**, *97*, 173–205.

[2] J. M. Tour, *Acc. Chem. Res.* **2000**, *33*, 791–804.

[3] M. A. Reed, T. Lee, *Molecular Nanoelectronics* **2003**, American Scientific Publishers, Los Angeles, California, (USA).

[4] M. C. Petty, M. R. Bryce, D. Bloor, *Introduction to Molecular Electronics* **1995**, Oxford University Press, New York.

[5] R. M. Metzger, *Chem. Rev.* **2003**, *103*, 3803–3834.

[6] D. K. James, J. M. Tour, *Chem. Mater.* **2004**, *16*, 4423–4435.

[7] R. L. McCreery, *Chem. Mater.* **2004**, *16*, 4477–4496.

[8] H. He, J. Zhu, N. J. Tao, L. A. Nagahara, I. Amlani, R. Tsui, *J. Am. Chem. Soc.* **2001**, *123*, 7730–7731.

[9] a) M. Brust, M. Walker, D. Bethell, D. J. Schiffrin, R. Whyman, *J. Chem. Soc. Chem. Commun.* **1994**, 801–802; b) M. Brust, J. Fink, D. Bethell, D. J. Schiffrin, C. Kiely, *J. Chem. Soc. Chem. Commun.* **1995**, 1655–1656.

[10] T. Ogawa, K. Kobayashi, G. Masuda, T. Takase, S. Maeda, *Thin Solid Films* **2001**, *393*, 374–378.

[11] a) K. Araki, H. Endo, G. Masuda, T. Ogawa, *Chem. Eur. J.* **2004**, *10*, 3331–3340; b) K. Araki, H. Endo, H. Tanaka, T. Ogawa, *Jap. J. Appl. Phys.* **2004**, *43*, L634–L636.

[12] a) J. Roncali, *Chem. Rev.* **1992**, *92*, 711–738; b) H. Shirikawa, E. J. Lewis, A. G. MacDiarmid, C. K. Chiang, A. J. Heeger, *J. Chem. Soc. Chem. Commun.* **1977**, 578–579.

[13] a) J. H. Liao, M. Benz, E. L. Goff, M. G. Kanatzidis, *Adv. Mater.* **1994**, *6*, 135–138; b) D. D. Graf, R. G. Duan, J. P. Campbell, L. L. Miller, K. R. Mann, *J. Am. Chem. Soc.* **1997**, *119*, 5888–5899; c) G. Barbarella, M. Zambianchi, L. Antolini, P. Ostoja, P. Maccagnani, A. Bongini, E. A. Marseglia, E. Tedesco, G. Gigli, R. Cingolani, *J. Am. Chem. Soc.* **1999**, *121*, 8920–8926; d) T. M. Barclay, A. W. Cordes, C. D. MacKinnon, R. T. Oakley, R. W. Reed, *Chem. Mater.* **1997**, *9*, 981–990.

[14] M. P. Samanta, W. Tian, S. Datta, J. I. Henderson, C. P. Kubiak, *Phys. Rev. B* **1996**, *53*, 7626–7629.

[15] a) Y. Yu, E. Gunic, B. Zinger, L. L. Miller, *J. Am. Chem. Soc.* **1996**, *118*, 1013–1018; b) L. L. Miller, Y. Yu, *J. Org. Chem.* **1995**, *60*, 6813–6819.

[16] S. M. Sze, *Physics or Semiconductor Devices* **1981**, 2nd ed., Wiley, New York.

[17] Y. Selzer, L. Cai, M. A. Cabassi, Y. Yao, J. M. Tour, T. S. Mayer, D. L. Allara, *Nano Lett.* **2005**, *5*, 61–65.

[18] Y. Chen, M. Zwolak, M. D. Ventra, *Nano Lett.* **2003**, *3*, 1691–1694.

[19] A. D. Schwab, D. E. Smith, B. Bond-Watts, D. E. Johnston, J. Hone, A. T. Johnson, J. C. de Paula, W. F. Smith, *Nano Lett.* **2004**, *4*, 1261–1265.

[20] P. K. Sudeep, B. I. Ipe, K. G. Thomas, M. V. George, *Nano Lett.* **2002**, *2*, 29–35.

[21] K. G. Thoms, P. V. Kamat, *Acc. Chem. Res.* **2003**, *36*, 888–898.

[22] S. Chen, R. W. Murray, *J. Phys. Chem. B* **1999**, *103*, 9996–10000.

[23] S. Barazzouk, P. V. Kamat, S. Hotchandani, *J. Phys. Chem. B* **2005**, *109*, 716–723.

[24] O. Pieroni, F. Ciardelli, *Trends Polym. Sci.* **1995**, *3*, 282–287.

[25] K. Okajimaa, H. Yamatsugub, C. Wenb, M. Sudoha, K. Yamadab, *Thin Solid Films* **2001**, *381*, 267–275.

[26] Unpublished results.

[27] Molecular structure Coorporation & Rigaku Coorporation **2001**. Crystalclear Version 1.3. MSC, 9009 New Trails Drive, The Woodlands, TX 77381–5209, USA, and Rigaku, Toyko, Japan.

[28] Molecular structure Coorporation & Rigaku Coorporation **2000**. TEXSAN Version 1.11. MSC, 9009 New Trails Drive, The Woodlands, TX 77381–5209, USA, and Rigaku, Toyko, Japan.

[29] Bruker **2000**. SHELXTL Version 6.10. Bruker AXS inc., Madison, Wisconsin, USA.